JOURNAL OF SOLID STATE CHEMISTRY **139,** 105–123 (1998)
ARTICLE NO. SC987815

Structural and Microstructural Aspects of $Si_x(Ta, Nb)Te_2$

N. Frangis,*,† G. Van Tendeloo,*,[1] C. Manolikas,† and S. Amelinckx*

*EMAT, University of Antwerp (RUCA), Groenenborgerlaan 171, B-2020 Antwerpen, Belgium, and †Solid State Physics Section, Department of Physics, Aristotle University of Thessaloniki, GR-54006 Thessaloniki, Greece

Received August 5, 1997; accepted March 17, 1998

The modulated structures of the compounds of the type A_xMTe_2 (M = Nb, Ta; A = Si, Ge) are discussed, and the electron diffraction patterns and high-resolution electron microscopy images are analyzed in terms of interface modulated structures. The structure of Si_xTaTe_2 ($x \approx 1/3$) is of particular interest; it results from the presence of periodic interfaces of two types leading to an incommensurately looking diffraction pattern with a q-vector slightly larger than $c_0^*/3$. A domain microstructure consisting of three orientation variants and three translation variants is revealed and interpreted in terms of the crystal structure. The domains are assumed to result from an order–disorder transition. In Si_xNbTe_2(x = 3/7), different long period structures with long periods $7c_0$, $8c_0$ and $9c_0$ are formed. Possible models are discussed.

INTRODUCTION

The structures of the A_xMTe_2 compounds (M = Nb, Ta; A = Si, Ge; $x \leq 1/2$) were determined by several authors (1–5), who agree on the ordered structure of the $x = 1/2$ compounds (see following discussion in "Structural Considerations" section).

The stoichiometric compounds with $x = 1/2$ have an orthorhombic superstructure of the β-MoS_2 sandwich-type structure, whereas the compounds with $x < 1/2$ have composition-driven long-period one-dimensional modulated structures derived from the ordered $x = 1/2$ structure. These long-period structures have also been studied by several authors (6, 7). It was suggested that they consist of modules of the $A_{0.5}MTe_2$ structure, with a width depending on the composition, separated by strips of the MTe_2 structure.

Because high-resolution electron microscopy (HREM) combined with electron diffraction is a powerful tool for the study of modulated structures, it was considered worthwhile to study these compounds in some detail with the emphasis on deviations from the average structures as determined by X-ray diffraction. Several new structural features which could be interpreted by extending the existing models were discovered. A remarkable microstructure was found and related to these structural models.

[1]To whom correspondence should be addressed.

EXPERIMENTAL

The materials were prepared following a method described in Refs. 2 and 4. In brief, a mixture containing the stoichiometric proportion of the elements (nominal compositions: $Si_{0.36}TaTe_2$ and $Si_{0.43}NbTe_2$) was heat-treated in evacuated sealed quartz tubes at 900°C during 10 days. Under these conditions small vapor-grown single crystals were obtained.

Because the materials exhibit a pronounced cleavage along the layer planes, specimens suitable for transmission electron microscopy were prepared by cleaving the crystals, using cellophane tape, and depositing the flakes on copper grids, using a cellophane tape glue solution. Specimens for cross-sectional observations were prepared by gluing flakes between two pieces of glass and then following the traditional procedure for cross-sectional thinning (i.e., mechanical polishing and ion beam milling). HREM images were obtained using a Jeol 4000EX microscope, having a Scherzer resolution of 1.7 Å.

STRUCTURAL CONSIDERATIONS

The structures of the compounds of the type A_xMTe_2 are derived from the structure of the trigonal prismatic MoS_2 prototype, which can be represented by the stacking symbol $A\gamma AC\alpha C\ldots$, where the Latin letters represent closely packed Te layers and the Greek letters represent the transition metal M-layers (Mo, Ta, Nb, …). In such a structure, half the trigonal prismatic interstices in a $A\gamma A$ sandwich are vacant (e.g., the ∇ oriented ones); the other half (e.g., the Δ oriented ones) are filled by Ta in γ positions. The filled interstices thus only share edges. Successive sandwiches are held together mainly by Van der Waals interaction.

0022-4596/98 $25.00

The addition of silicon (or germanium) has two consequences (1, 2). These tetravalent ions do not intercalate in the Van der Waals gap as Co, Ni, or Fe do, but instead they enter the sandwich and occupy sites with a square planar configuration. Such sites are available in the centers of side faces of the trigonal prisms. As a result, the pair of face-sharing adjacent (Δ and ∇) interstices, separated by the square planar configuration, remain vacant. This causes Ta ions from half these trigonal prismatic interstices to go into similar vacant sites, adjacent to an already occupied one, leading to the formation of "pairs" of Ta ions in face-sharing pairs of Δ and ∇ prismatic interstices. We call this the basic superstructure (SS); it is shown schematically in Fig. 1. Its structure is orthorhombic with lattice parameters $a_0 = 6.329$ Å, $b_0 = 14.0$ Å, $2c_0 = 7.65$ Å.

In a compound with ideal composition ($x = 1/2$), all Ta ions would form such pairs. However in nonstoichiometric compounds with $x < 1/2$, a number of Ta ions remain in isolated (edge-sharing) trigonal prismatic interstices. One can then distinguish two types of tantalum ions in trigonal prismatic interstices; "isolated" ones and "paired" ones.

We have as yet ignored the deformation of the Te sublattice as a result of the pairing of the Ta ions. It is to be expected that within a sandwich the Ta ions in face-sharing trigonal prisms repel one another rather strongly giving rise to an elongation of the rhombic section of the face-sharing pair of trigonal prisms. In the structure (Fig. 2) such pairs enclose an angle of about 30° with the c-direction. Their repulsion will thus result in a decrease of the a/c ratio ($a/c = 1.652$) as compared to that in the ideal hexagonal arrangement ($a/c = 1.73$). The "isolated" tantalum ions form a zig-zag arrangement of edge-sharing prisms, separating strips which exhibit the structure of the "basic" compound with ideal composition ($x = 1/2$) (Fig. 1). The periodic presence of these zig-zag arrangements accounts for the nonstoichiometry; their average separation determines the actual composition and the long spacing. A schematic representation of one sandwich is shown in Fig. 3. Note the continuity of the sublattice of Te ions across the whole area. In actual fact, the Te sublattice is periodically deformed (6), but we ignore this in the present discussion. The structure in which these zig-zag arrangements occur periodically (ideally with a period $3c_0$) will be referred to as the long-period superstructure (LPSS), with a long parameter $3c_0 = 11.48$ Å.

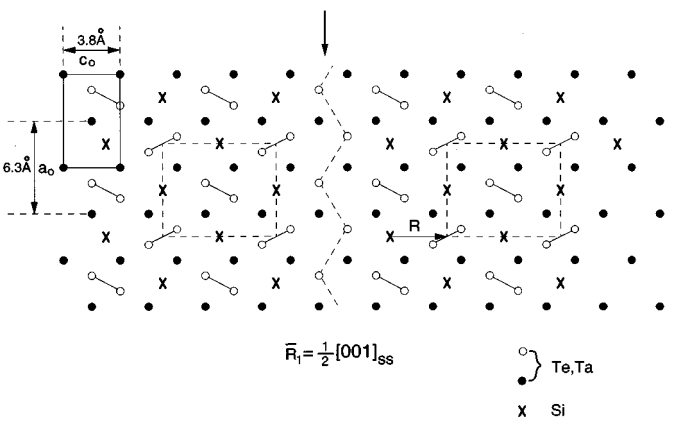

FIG. 1. Schematic representation of one sandwich of the basic structure of $Si_{0.5}TaTe_2$. A unit mesh of the SS is outlined. Pairs of Ta ions are connected by a line segment. The crosses mark the silicon positions. One out-of-phase boundary (OPB) with $\bar{R}_1 = \frac{1}{2}[001]_{SS}$ is present along the zig-zag line marked by an arrow. Isolated Ta ions occur along the OPB.

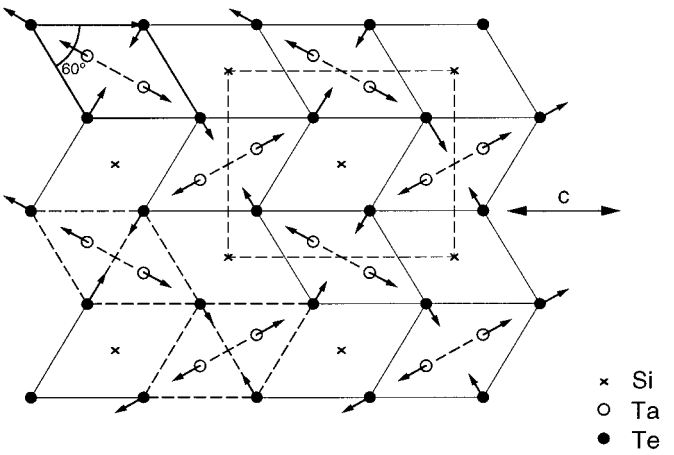

FIG. 2. Strain pattern of the basic hexagonal lattice of $TaTe_2$ resulting from Ta–Ta pair formation as a consequence of the addition of Si. The arrows indicate the directions of the forces within Ta–Ta pairs, which form elastic dipoles. The ordering of these dipoles causes an increase of the c parameter.

It is clear that within the same hexagonal Te sublattice ($a_0 = 6.329$ Å; $c_0 = 3.8258$ Å), these zig-zag arrangements can adopt three symmetry-related directions, enclosing angles of 120° (or 60°), which will lead to a striking domain structure as we shall see later.

The sandwiches are stacked according to the …/AABB/AABB/… mode (β-MoS_2 type) leading to two sandwiches per unit cell. The presence of the zig-zag line of isolated Ta ions makes a different stacking modes possible, depending also on the separation between such zig-zag lines within the same sandwich, [i.e., on the value of x as well as on the projected relative positions of the "zig-zag" lines (i.e., the OPBs) in successive sandwiches].

From Fig. 3 it is clear that the strips of $MA_{0.5}Te_2$ structure are related by a displacement over $\bar{R}_1 = (\frac{1}{2})[001]_{SS}$ when referred to the basic superstructure. We shall use the term out-of-phase line for this zig-zag line.

The presence of the zig-zag lines creates an anisotropy and contributes in reducing the symmetry to orthorhombic

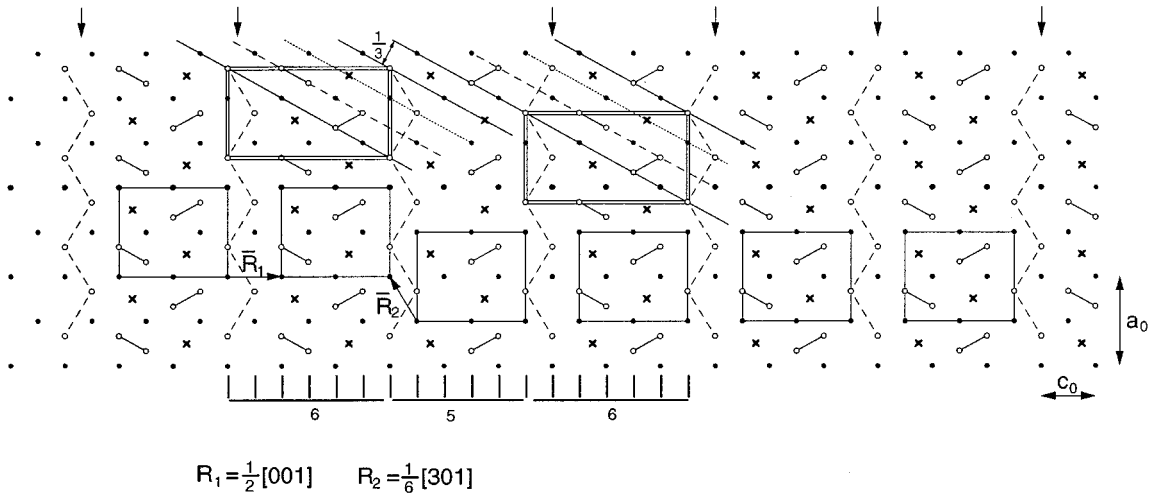

FIG. 3. (010) projection of the structure in a sandwich. The model consists of a sequence of OPB's with a displacement vector $\bar{R}_1 = \frac{1}{2}[001]_{SS}$ separated by six interplanar distances of the Te sublattice, leading to an LPSS of which the unit mesh is indicated by double lines. A singular domain strip with a width of five interplanar distances of the sublattice is shown as well. Note the lateral 1/3 offset of the $[101]_{LPSS}$ and $[10\bar{1}]_{LPSS}$ rows of atoms at this singular strip, which is caused by the presence of an OPB with $\bar{R}_2 = \frac{1}{6}[301]_{LPSS}$.

and increases the c parameter. Because these "lines" are nonconservative, their presence changes the composition.

The diffraction pattern suggests that the actual structure of Si_xTaTe_2 is closely related to this commensurate LPSS but is more complicated by the periodic presence of a second type of OPB leading to a very-long-period superstructure (VLPSS) producing an incommensurately looking diffraction pattern.

THE Si_xTaTe_2 STRUCTURE

Long Period and Composition

The composition per unit length along the a-direction of the basic superstructure is $MA_{0.5}Te_2$, whereas the composition of the inserted strip along the out-of-phase boundary is MTe_2. As a result, when the separation of the OPBs in a sandwich is $(n + 1)c_0$ (i.e., when n unit cells of the basic superstructure are followed by one MTe_2 strip), the corresponding composition is $n(A_{0.5}MTe_2) + MTe_2 = A_{n/2}M_{n+1}Te_{2n+2}$ and the period along c then becomes $(n + 1)c_0$. If the sequence is an alternation of strips of two different widths m and n (m, n = even), the corresponding composition is $(m + n)(A_{0.5}MTe_2) + 2MTe_2 = A_{(m/2)+(n/2)}M_{m+n+2}Te_{2(m+n+2)}$ and the period along c now becomes $(m + n + 2)c_0$. The idealized LPSS ($n = 2$) thus has a period of $3c_0$ and a composition $A_{1/3}MTe_2$.

A full description of the spatial structure requires the stacking of the sandwiches. In particular, the projected period along the [010] zone would be halved, as compared to that in a single sandwich, if the OPB lines in successive sandwiches would be in relative positions such that an A-centered arrangement would result, with all zig-zag lines "in phase." The diffraction patterns along [100], discussed later, show the A-centering in Si_xTaTe_2.

Diffraction Patterns

A typical electron diffraction pattern of Si_xTaTe_2 along the [010] zone, indexed with respect to the LPSS unit cell outlined by double lines in Fig. 3, is shown in Fig. 4a. The reciprocal unit mesh, corresponding to the orthorhombic unit mesh of the underlying $TaTe_2$ structure in direct space, consists of the most intense spots and is outlined in Fig. 4a. This unit mesh is centered, as is the corresponding unit mesh (a_0, c_0) in direct space. A magnified pattern of Fig. 4a, showing the spot splitting in more detail is represented in Fig. 5a and schematically in Fig. 5b. Figure 5b also shows the traces of a number of sections of reciprocal space, which are reproduced in Fig. 4b–e. In particular Fig. 4e shows that the [100] zone is A-centered. Figure 4b and d show the extinctions of the spots $0k0$ with k = odd; the presence of weak spots of this type are caused by double diffraction. The intense streaking in Fig. 4c suggests that a one-dimensional stacking disorder sometimes occurs along the b_0 axis.

Each of these intense spots in Figs. 4a and 5a is the origin of a sequence of equispaced satellite spots corresponding approximately to a threefold period $3c_0$, the wavevector

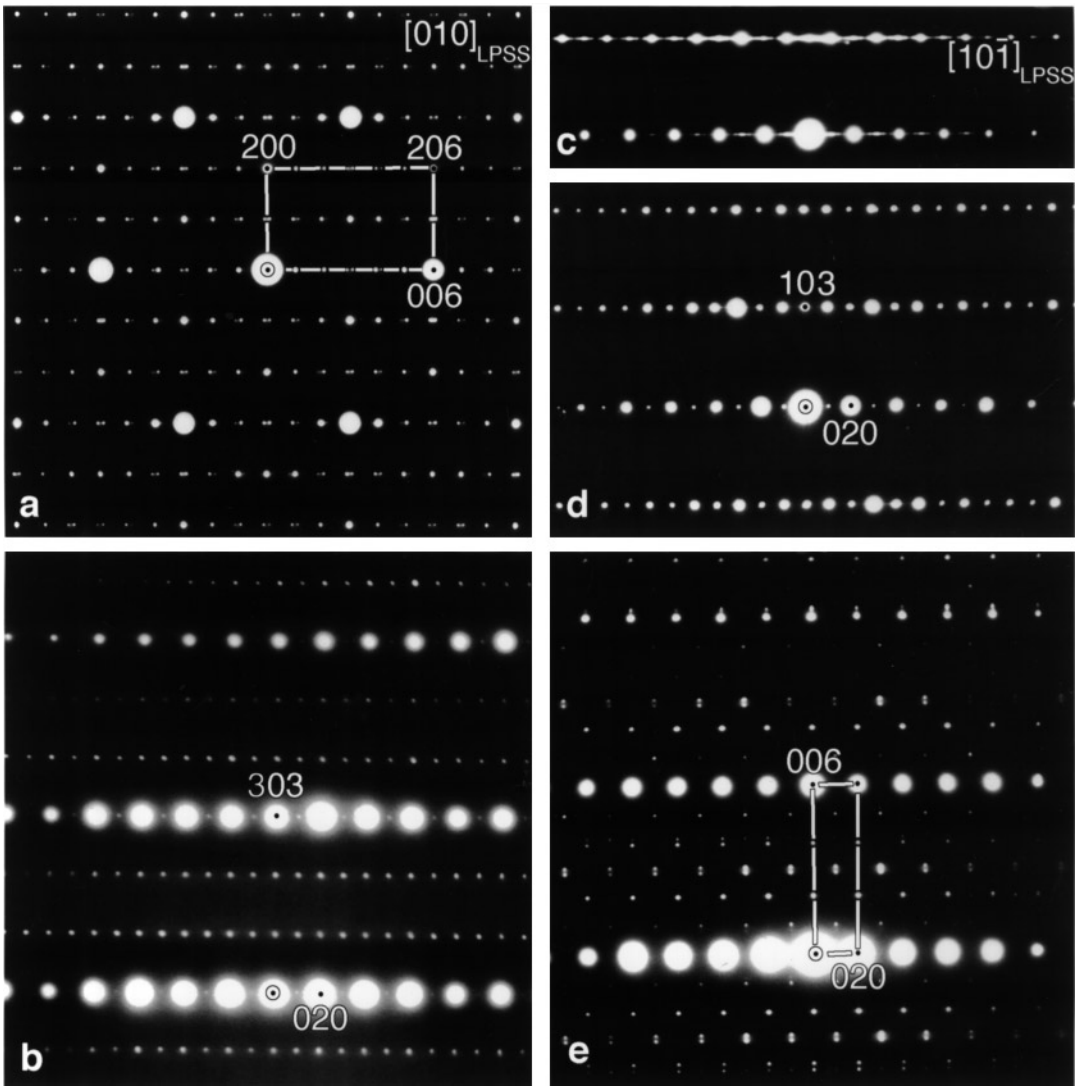

FIG. 4. Diffraction patterns of Si_xTaTe_2 along different zone axis indexed with reference to the LPSS. (a) $[010]_{LPSS}$ zone axis. (b) $[30\bar{1}]_{LPSS}$ zone axis (section 2 in Fig. 5b). (c) $[10\bar{1}]_{LPSS}$ zone axis, [compare streaked pattern with (d)]. (d) $[10\bar{1}]_{LPSS}$ zone axis (section 1 in Fig. 5b). (e) $[100]_{LPSS}$ zone axis, which reveals the long period as well as stacking of the sandwiches (section 3 in Fig. 5b).

q being slightly larger than $1/3c_0^*$. However in actual fact, the pattern is incommensurate as is evident from the "spacing anomaly"; the real modulation period is slightly smaller than $3c_0$. A straightforward interpretation would be to attribute this spacing anomaly to a uniform mixture of two different spacings between all identical 'zig-zag' lines (i.e., OPB lines): $3c_0$ with a small admixture of $2c_0$. However, as we shall see, the high-resolution images suggest another model involving a VLPSS resulting from the periodic presence of a second type of OPB in the idealized LPSS.

There are no "fractional shifts" (8) of the satellite sequences in Fig. 4a with respect to the basic spots; this is consistent with most types of modulation (Fig. 5b). However, because several satellites have an appreciable intensity (four or five on each side of the basic spots), the modulation must include several higher harmonics. It is therefore a reasonable approximation to consider a stepwise modulation resulting from planar interfaces. In the present case, the interfaces have a certain width because they are nonconservative. One such interface is shown in Fig. 1. Successive strips of the basic ordered structure are related by a displacement vector $\bar{R}_1 = \frac{1}{2}[001]_{SS}$. This leads to $\bar{g}\cdot\bar{R}$ values which are integers for all basic spots $\bar{g}$ of the SS, which is consistent with the absence of fractional shifts (see Fig. 5b).

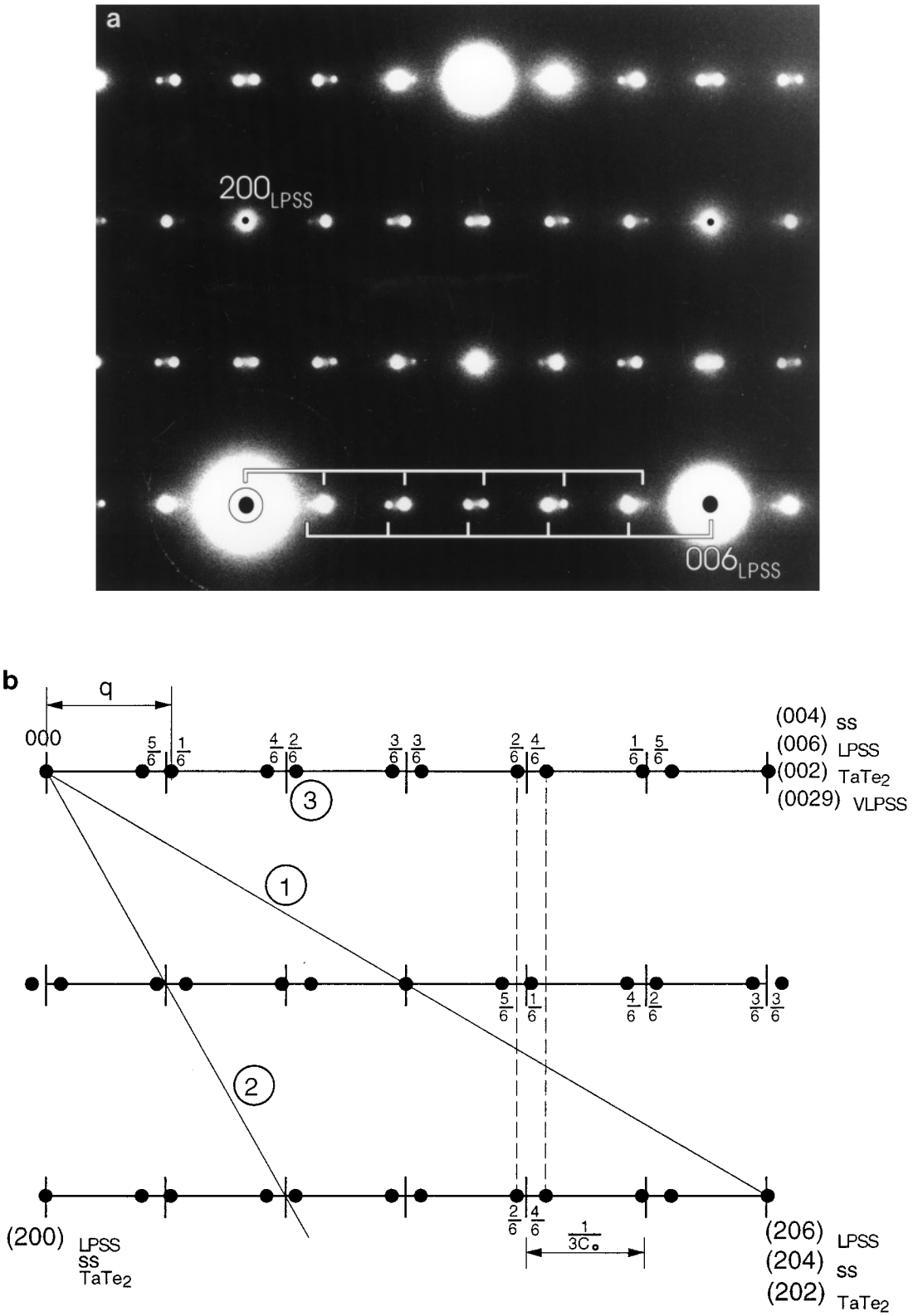

FIG. 5. (a) High magnification of part of the [010] DP of Fig. 4a. (b) Schematic representation of (a) indexed in terms of three different reference frames. Note the fractional shifts over multiples of 1/6 with respect to spot positions of the ideal LPSS, indicated by short bars. The spots of the VLPSS form a centered rectangular arrangement as indicated by one rectangle. The sections of the reciprocal space giving rise to the diffraction patterns of Fig. 4b, d, and e are indicated.

High-Resolution Observations

Because the geometry of the three sublattices of Te, Ta, and Si within the same sandwich are different, it is possible to conclude from geometrical considerations which subset of atom columns is being revealed in the image. The images are of a sufficiently good quality to ensure that all atom columns of the same subset will be imaged similarly. This is due to the fact that the material has a very pronounced cleavage parallel to the (010) plane and therefore thin planar specimens of constant thickness can conveniently be obtained; contrast changes due to thickness variation can be neglected.

In exceptionally thin samples, all heavy atom columns in the structure are imaged under suitable defocus conditions as in Fig. 6. The geometry of the pattern of bright dots corresponds to the pattern of atom columns in the two superposed sandwiches. This requires optimum imaging conditions as well as very thin samples; the separation of these atom columns (2.1 Å) is of the same order as the resolution limit of the microscope (1.7 Å). Under the same imaging conditions, in adjacent regions, presumably with a slightly different thickness, prominently bright dots reflect the geometry of the hexagonal channels in the structure (Fig. 6a). As a result of this superposition the channels which were empty in a single sandwich now also contain cations in projection. Only image simulations can settle this point, as discussed later. The geometry of these channels is the same as that of the tellurium sublattice in a simple sandwich. Under spatially constant imaging conditions, it is thus possible to use this pattern of prominently bright dots to position the structure, especially because only relative positions of strips of a known basic structure are required to demonstrate the validity of the model for the long-period superstructure.

In the image of Fig. 7, all bright dots are located on a pseudo hexagonal lattice with a mesh shape and lattice parameters compatible with the Te configuration in one sandwich. It is therefore assumed that here the Te column sublattice is imaged as bright dots. Brightness variations can be attributed to the superposition of the two sandwiches which both have a slightly deformed Te sublattice (7).

Dark strips parallel to [100] in which the dot brightness is relatively much smaller, must be attributed to the out-of-phase lines; they are indicated by white bars in Fig. 7. This interpretation is based on the observation that their spacing is the same as that of the OPBs in the model. Their geometry is again consistent with the assumption that the bright dots image tellurium columns. The out-of-phase strip contains one [100] row of Te columns less (5 instead of 6) (Fig. 3). Such anomalous strip widths occur periodically alternating with blocks of four (or sometimes five) strips of normal

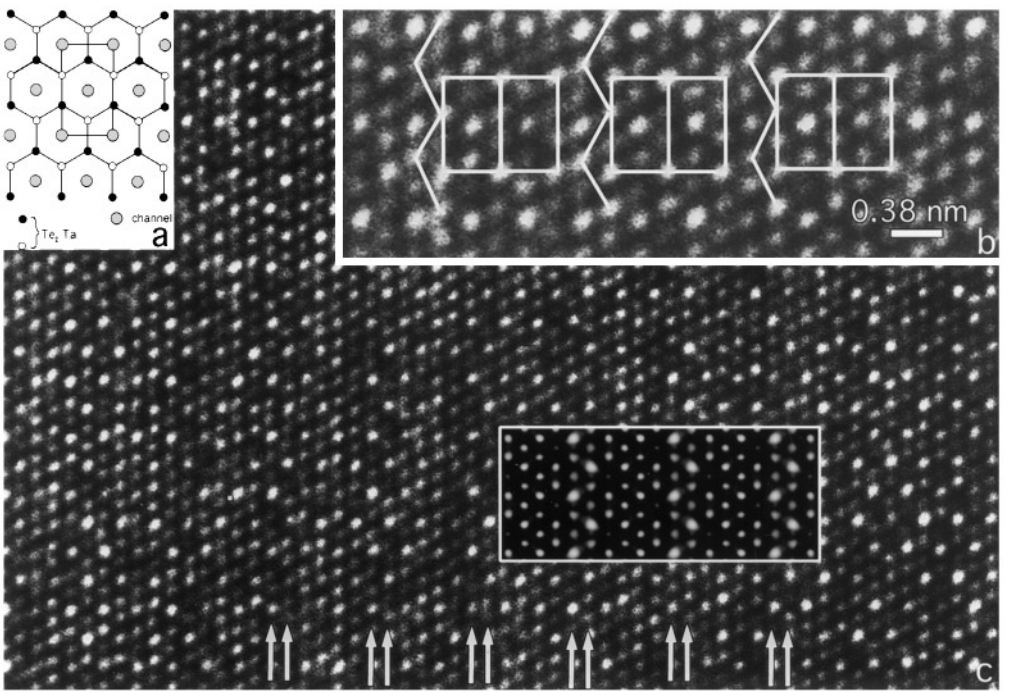

FIG. 6. [010] high resolution image of Si_xTaTe_2. (a) Projected arrangement of the $TaTe_2$ columns, showing also the arrangement of the channels in the structure; these channels are occupied by Ta and Si in the superstructures. (b) High-magnification image with superimposed model. All atom columns, as well as the channels are revealed. (c) Lower-magnification image; the arrows indicate the positions of the zig-zag chains of Ta pairs. The simulated image, shown as an inset (thickness, 49 Å; focus, 1000 Å) was calculated for the LPSS structure.

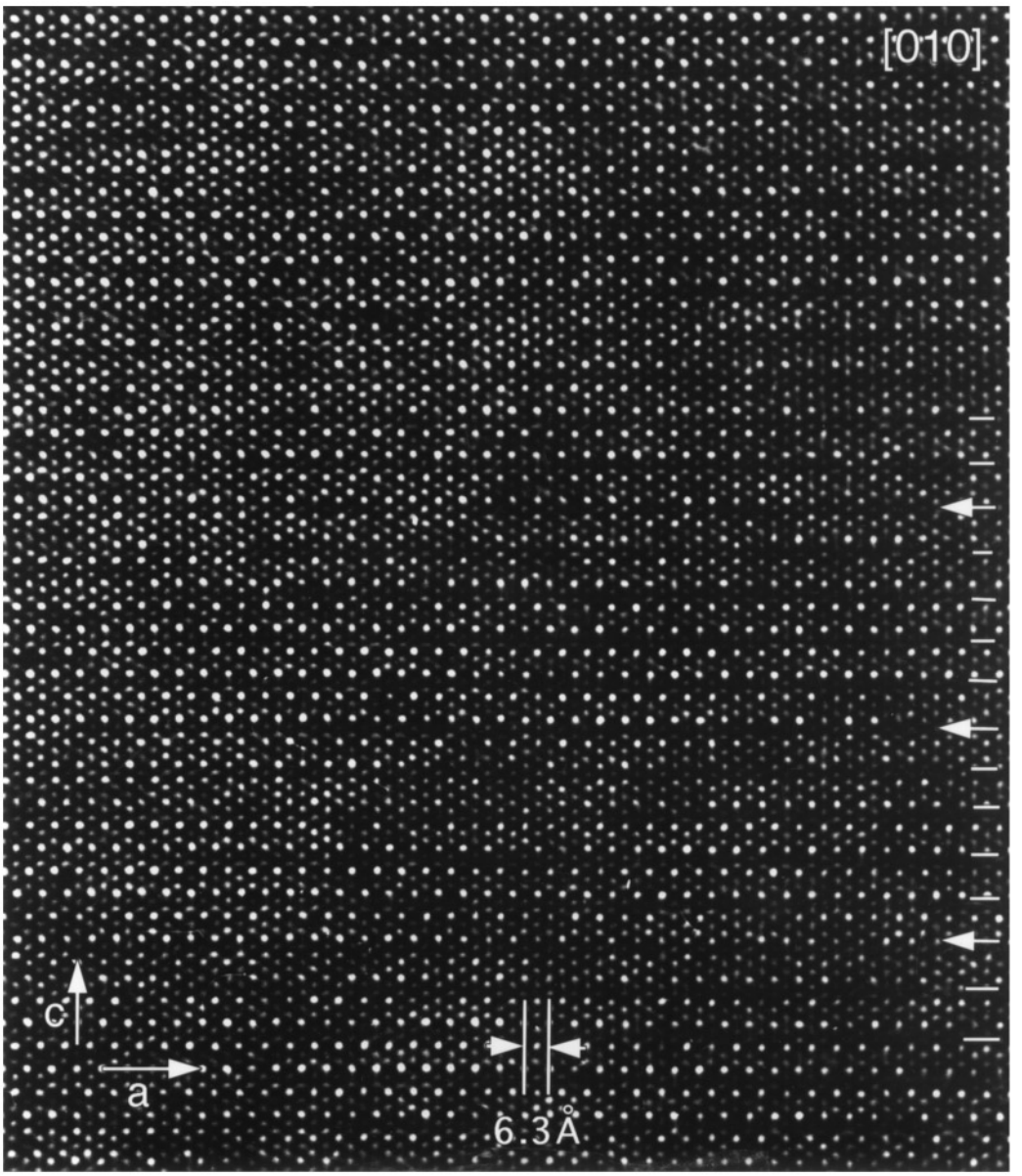

FIG. 7. High-resolution image along the [010] zone. The dense hexagonal net of bright dots reveals the Te sublattice. The dark lines indicated by white strips image OPBs of the LPSS. Note that the rows of extra bright dots are laterally shifted over $\frac{1}{3}$(mod 1) of the interrow distance along the singular OPBs of the VLPSS; they are indicated by a larger arrow.

width. This leads to an average long period of $[(4 \times 6) + (1 \times 5)]/5 = 5.8$ or a q-vector $q = 0.3448\ c_0^*$ which is consistent with the q-value of $0.3446\ c_0^*$ deduced from the diffraction pattern of Fig. 5b.

The "anomalous" strips with a width of five rows (instead of six) also introduce an "out-of-phase" relationship between the LPSS left and right of it, laterally shifting the prominently bright dot rows parallel to $[101]_{LPSS}$ and $[10\bar{1}]_{LPSS}$ over 1/3 of the interrow spacing along this direction. They are indicated by arrows in Fig. 7 but are much more visible on an inclined photograph along one of these directions in Fig. 8. A super-superstructure is thus formed as a result of the presence of out-of-phase lines which have periodically a deviating spacing and also a different displacement vector $\bar{R}_2 = \frac{1}{6}[301]$. The q-vector derived from the diffraction pattern is in close agreement with the modulation period derived from the direct space images ($q = 0.345\ c_0^*$). The model therefore seems to be consistent.

The cross-sectional image of Fig. 9, along with section 2 in Fig. 5b, shows the stacking of the sandwiches: it is

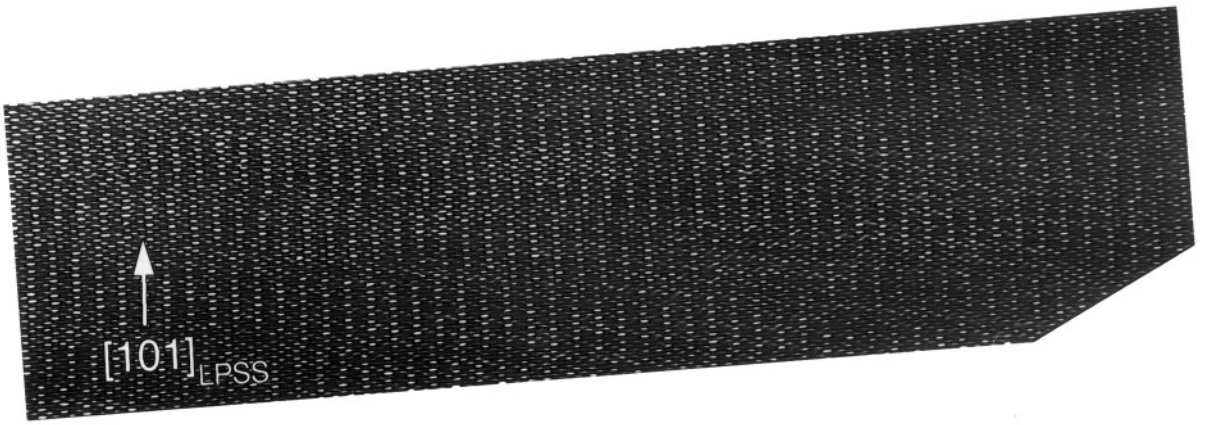

FIG. 8. For shortened view of Fig. 7 made under grazing incidence, showing clearly the lateral offset of the extra bright dot rows along $[101]_{LPSS}$ (and $[10\bar{1}]_{LPSS}$) directions.

consistent with the $A\gamma AC\alpha C$ stacking. The Te and Ta columns are apparently imaged here as dark dots; the bright lines must be associated with the Van der Waals gaps.

The Microstructure

Many crystals exhibit a remarkable domain structure of which Fig. 10 is an example observed under high-resolution conditions.

Topologically similar domain structures were observed in $NbTe_2$ (9), $Pb_3(VO_4)_2$ (10) and $MoTe_2$ (11). In all these cases, the domain fragmentation was a consequence of the decrease in symmetry accompanying a second-order phase transition from a hexagonal parent phase into a phase of either monoclinic or orthorhombic symmetry. This gives rise to either six or three symmetry-related orientation variants. The resulting microstructure is such as to minimize the elastic energy associated with the transformation strains.

The observation of a number of similar configurations in the present material and in particular the occurrence of three different orientation variants suggests that the "parent" phase in this case is also hexagonal and that at some stage a transition took place into an orthorhombic structure. This transition is presumably associated with the ordered "pairing" of the Ta ions, which in turn is a consequence of the presence of the Si atoms within the sandwich. It is therefore suggested that at some stage in the growth process, perhaps close to the melting point of the compound, the silicon atoms are disordered in the hexagonal $TaTe_2$ matrix with correspondingly disordered Ta pairs. The presence of the Ta ions in the face-sharing pairs of trigonal prisms creates an elastic dipole because the tantalum ions repel each other. On cooling, these dipoles tend to order in their mutual stress fields and in doing so give rise to a configuration in which the compressively strained regions overlap to the largest possible extent regions of dilatational strain. This leads to the configuration of Fig. 2, which occurs in the actual superstructure and causes also some deformation modulation of the Te sublattice.

Using the lattice of one of the variants as a reference frame, the directions of the OPB lines in the other two variants are along $[101]_{LPSS}$ and $[10\bar{1}]_{LPSS}$. However, it is more illustrative to ignore first the orthorhombic deformation and to refer the three variants to the hypothetical parent structure, assuming the latter to be hexagonal. Figure 11 shows the Te sublattice of the three variants superposed on the lattice of the parent hexagonal phase.

The interfaces between variants are visibly coherent reflection twins (Fig. 10); the long-period directions enclosing angles of 120° (or 60°). In this hexagonal lattice, two sets of mirror planes (m_1, m_2, m_3) and (m'_1, m'_2, m'_3) can occur (Fig. 11). On this hexagonal lattice, the q-vectors may adopt three (six) orientations, indicated by their unit vectors in Fig. 11; the same directions are also traces of one set of symmetry planes. The second family of mirror planes m'_1, m'_2, m'_3 is indicated as well.

According to this model the OPBs, which are perpendicular to the q-vectors, also enclose angles of either 60° (e.g., q_1 and q_2) or 120° (e.g., q_1 and q_3). This however is an idealization which ignores the orthorhombic deformation. As we will see, this deformation will change the angles by a few degrees ($\sim 3°$).

The number of different orientation variants (3) is given by the order of the pointgroup of the parent phase ($6/m\ 2/m\ 2/m$; order 24) divided by the order of the point group of the product phase ($2/m\ 2/m\ 2/m$; order 8) (12). The different orientation variants are related by the symmetry elements which are lost on ordering. In the present case, they are the symmetry planes of $6/m\ 2/m\ 2/m$ which belong to the two

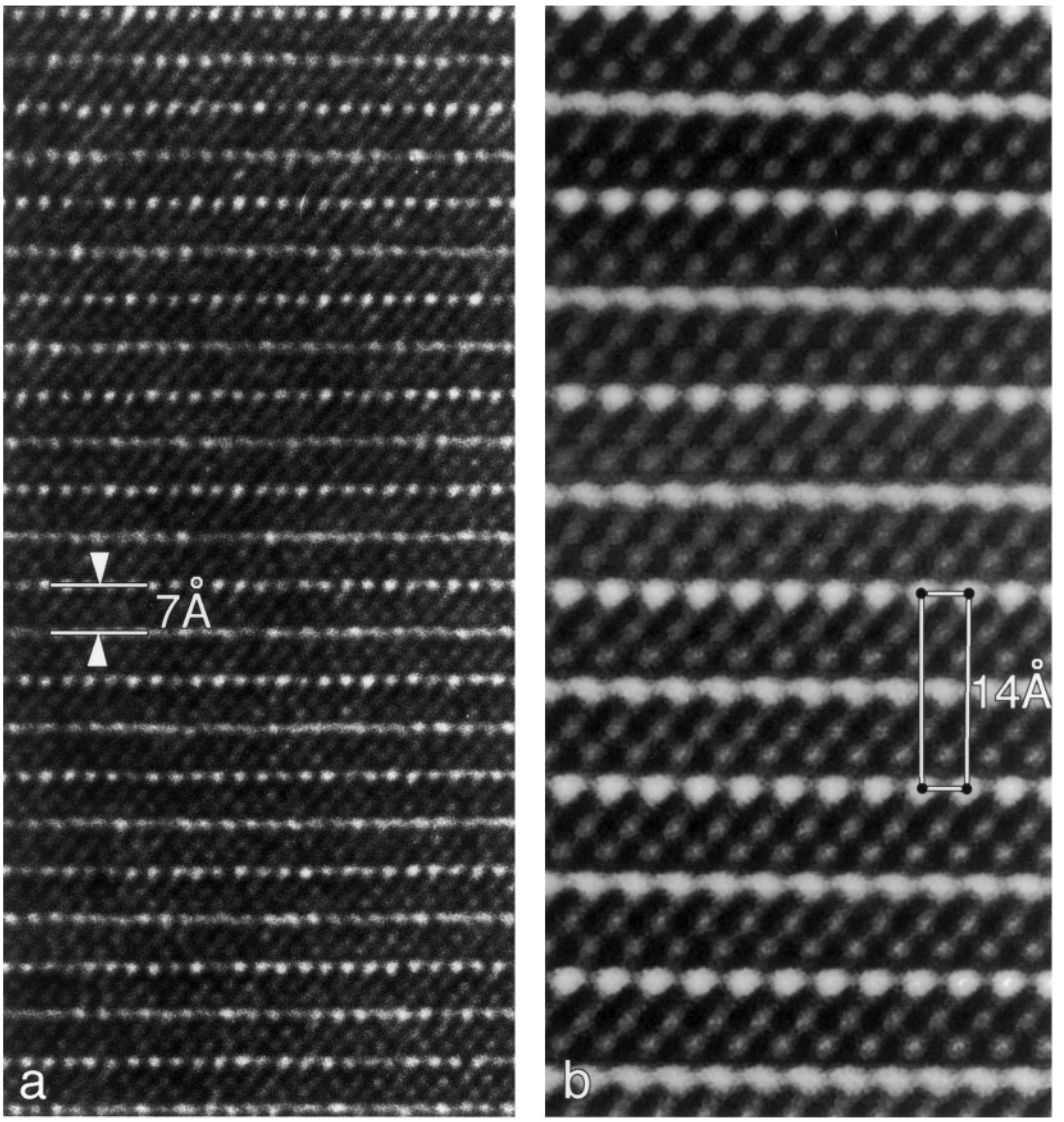

FIG. 9. (a) Cross-sectional view of the structure, as seen along the closely packed Te rows. The $A\gamma AC\alpha C$ stacking is revealed. The heavy atom columns are imaged as dark dots. The Van der Waals gap is imaged as a bright line. (b) Computer averaged image of (a) showing clearly the stacking.

sets mentioned earlier and one can thus expect two types of twins. For the first kind, the two domains have, for instance, q-vectors q_1 and q_2 related by the m_3. The trace of the twin interface is then either m_3 or m'_3. In the second kind (e.g., q_1 and q_3, related by m'_2), the trace of the interface is either m_2 or m'_2.

The coherent twin interfaces are the planes along which the two orthorhombic variants fit strainfree; this is shown in Fig. 12a and b. They are determined by symmetry and are thus to a large extent independent of the actual lattice parameters of the orthorhombic phase (13). This is the reason why configurations with the same topology occur in a variety of materials provided the point symmetries of the parent phase and the product phase are the same.

Figure 13 is a remarkable example of the domain structure imaged along the [010] axis. Similar features have previously been observed in the case of $Pb_2(VO_4)_3$ where they result from the $\gamma \rightarrow \beta$ phase transition; they have been called "stars" and "fans" in Ref. 9. Figure 13 contains a star as well as a fan. The separation of the fringes is that of the LPSS of $TaSi_xTe_2$ ($\approx$11.4 Å). These patterns involve two types of coherent twin boundaries which are parallel to the mirror planes of the hypothetical disordered hexagonal parent phase. These two types of boundaries are represented schematically in Fig. 12a and b, where it was assumed that

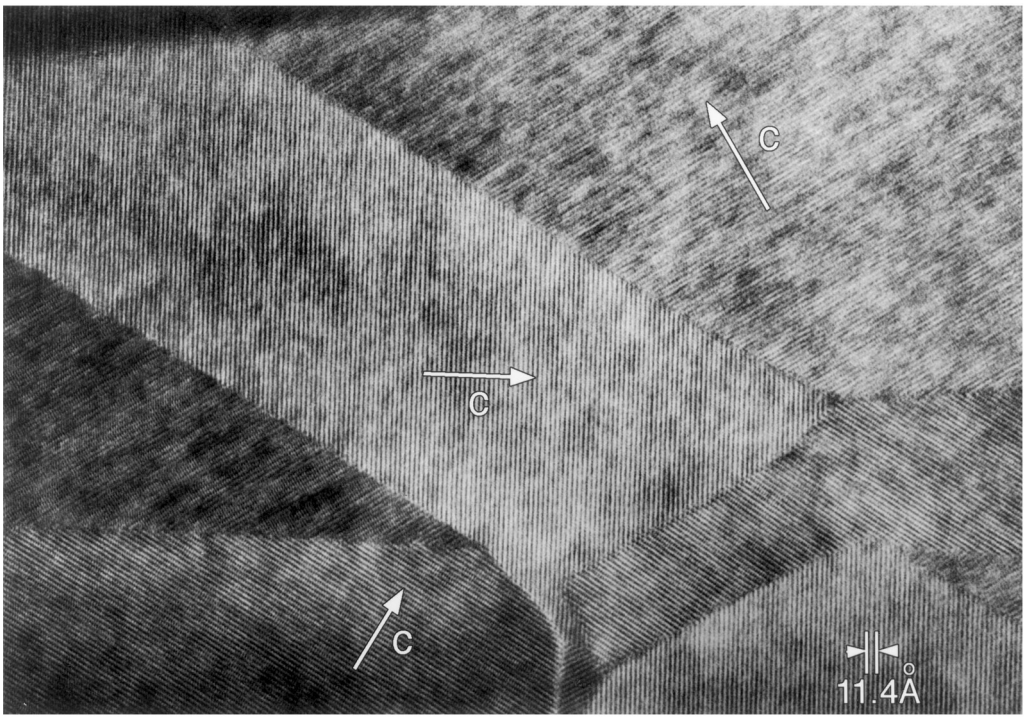

FIG. 10. Domain structure imaged in the high-resolution mode. The fringes reveal the LPSS; the interfringe distance along the [001] direction is 11.4 Å.

the tellurium sublattice is still undeformed, but that the ordering has taken place already. In actual fact, as a result of the deformation resulting from the ordering, the c parameter will become larger, and hence the angles θ_1 and θ_2 will become somewhat larger ($\sim 3^\circ$) than 120° and 60°, respectively. Homologous angles in the basic structure (e.g., the acute angle enclosed by the two c axes) then change in the opposite sense. A strain-free configuration can thus be obtained if around each node of domain walls an even number of twins corresponding to opposite angular strains will alternate. Except for its central area this is the case in the star pattern of Fig. 13. Also in the fan pattern, the ordering strains are minimised in this manner.

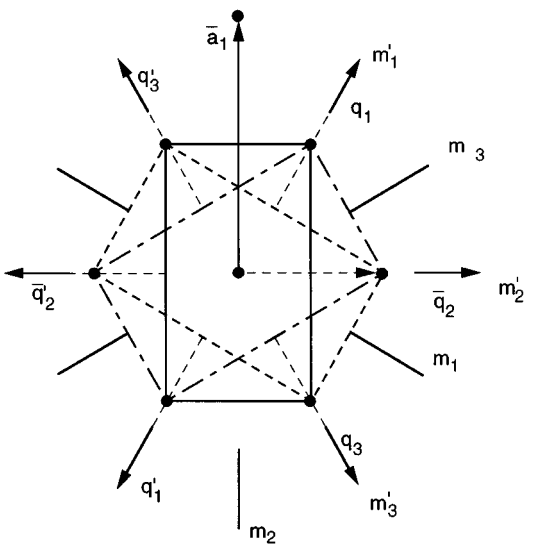

FIG. 11. Schematic diagram illustrating the twinning elements of the domain microstructure. There are two families of mirror planes: m_1, m_2, m_3 and m'_1, m'_2, m'_3.

In certain crystal parts of Si_xTaTe_2 the "dark lines" marking the positions of the periodic OPBs reveal some disorder in the LPSS. The dark lines appear to be shifted laterally in adjacent regions of the crystal (right part of Fig. 14). The boundary between such regions is somewhat diffuse and the "dark lines" are absent in the transition region. This boundary clearly separates two crystal regions in which the long-period superstructure has been formed in two different "phases" within the same continuous Te sublattice. In Fig. 15 such a boundary with a displacement vector $\frac{1}{6}[301]_{\mathrm{LPSS}}$ is represented schematically. Disordered arrays of such boundaries cause streaking along [100]* of the type observed in Fig. 16d.

In each of the three orientation variants, three different translation variants are thus possible for the LPSS; the considered boundaries separate two of these. The boundaries occur isolated, but they have the same type of displacement vector as the periodic ones giving rise to the VLPSS.

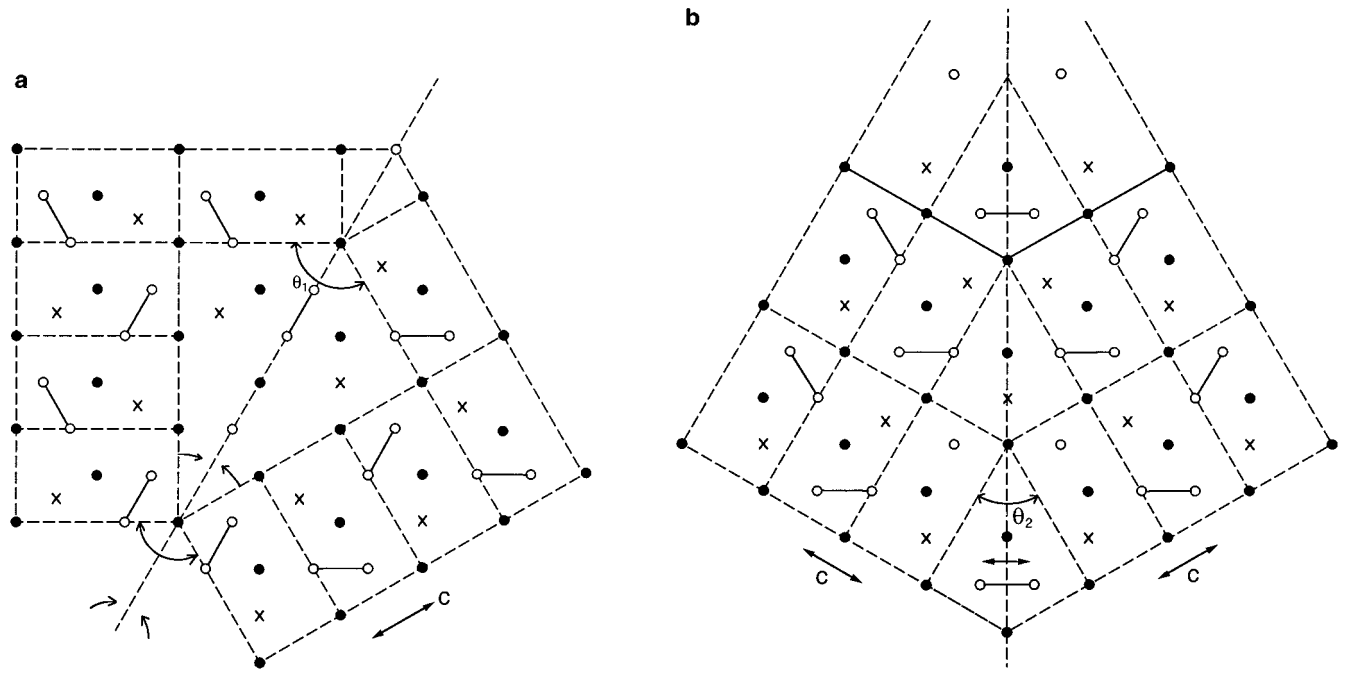

FIG. 12. Models for the two different types of coherent twins occurring in the $A_{0.5}MTe_2$ structure (SS). Note the continuity of the Te sublattice which is assumed to have remained hexagonal in the drawing. The ordering strains change the angles ($\theta_1 = 120°$ and $\theta_2 = 60°$ into $\theta'_1 = 123°$ and $\theta'_2 = 63°$). (a) Type I, with mirror plane m_1, m_2, or m_3. (b) Type II, with mirror plane m'_1, m'_2, or m'_3.

THE Si_xNbTe_2 ($x \approx 0.4$) STRUCTURE

The basic ordered structure of Si_xNbTe_2 is topologically the same as that of Si_xTaTe_2 (2, 4). However the superstructures (LPSS) are found to be different; they are generally commensurate but they can be derived from the basic ordered superstructure (SS) in much the same way as for the tantalum homologue.

Diffraction Patterns

Most relevant are the [010] zone patterns which exhibit the long-period structures. Three different [010] zone patterns are shown in Fig. 16. The centered rectangle of most intense spots corresponds again to the reciprocal of the unit mesh of the tellurium sublattice. The distance, along the densely populated rows of spots, from the origin to the first intense spot is divided in seven equal parts in Fig. 16a and nine equal parts in Fig. 16b. The spot pattern has a rectangular primitive unit mesh. Relatively more intense spots occur in the vicinity of the spot positions as a result of the basic superstructure (SS) with period c_0. This pattern is represented schematically in Fig. 17, where the short bars indicate the positions of the basic superstructure spots. The 0 0 4 spot of the basic structure must be indexed 0 0 14 (or 0 0 18) in the long-period superstructure.

In Fig. 16c, the superlattice spot spacing corresponds approximately to a repeat distance of 16 times the separation of tellurium rows. This suggests that the OPB would on the average be separated by the width of 8 tellurium unit cells (i.e., $8c_0$). We shall see below that a 1 : 1 mixture of 7 and 9 such spacings is more probable.

At variance with the situation in the incommensurate tantalum homologue, all LPSS spots are of comparable intensity. This is a consequence of the commensurate character of the superstructure which allows dynamical scattering to redistribute and average out the intensity differences.

Models

A model for one of the LPSS ($7c_0$) is shown in Fig. 18. It is clearly based on the same basic superstructure as Si_xTaTe_2. It consists of strips of this superstructure with a width of 6 (or 8 for the $9c_0$ LPSS) tellurium unit meshes, separated by OPB regions with a width of one tellurium unit mesh. The OPBs have the same configuration as in the homologous Ta compound; the equivalent displacement vector is again $\frac{1}{2}[001]_{SS}$. The fractional shifts are represented on the right of Fig. 17. The LPSS spots closest to the basic spot positions (SS) are clearly the most intense ones as expected for a periodic OPB modulated structure. This is represented schematically in Fig. 17 as dots of different sizes. All OPBs are

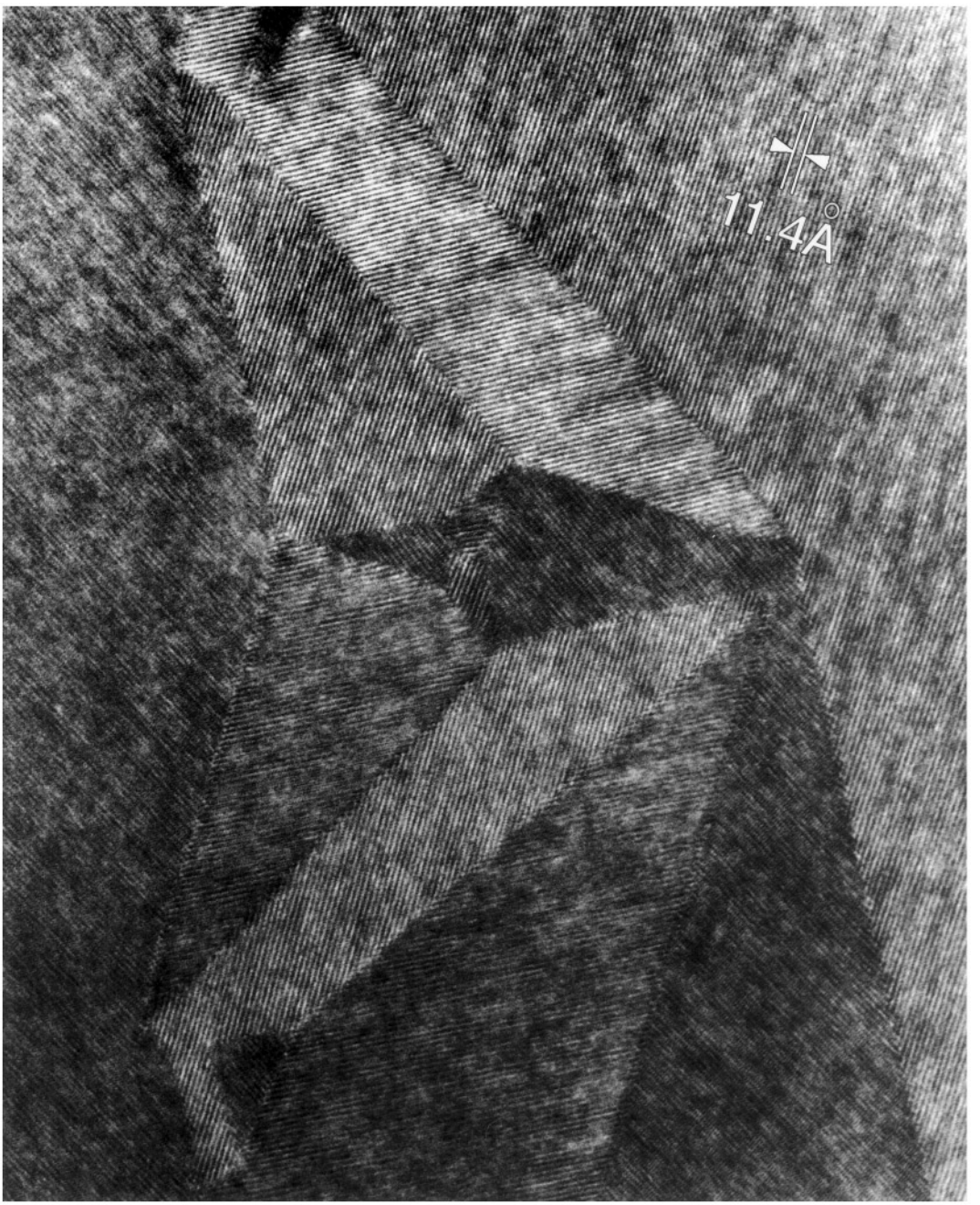

FIG. 13. Domain configuration exhibiting a fan pattern and a star pattern, imaged by the LPSS fringes.

identical and in phase, and they are separated by an odd number of Te unit cells (7 or 9).

High-Resolution Images

In Fig. 19, corresponding to a diffraction pattern exhibiting a $7c_0$ spacing, the periodic pattern of dark lines contains two dark lines in each period, as indicated by arrows. It is suggested that they correspond to the projections of OPB lines in the two superposed sandwiches of the unit cell. Note that no lateral offset is observed along any dot direction; this is a significant difference from the Ta case.

Figure 20 refers to Si_xNbTe_2; nominally the composition of the sample is $x = 3/7$, which would lead to a $7c_0$ long spacing. However, the corresponding diffraction pattern (Fig. 16c) exhibits a long period of $8c_0$. The rapid decrease in

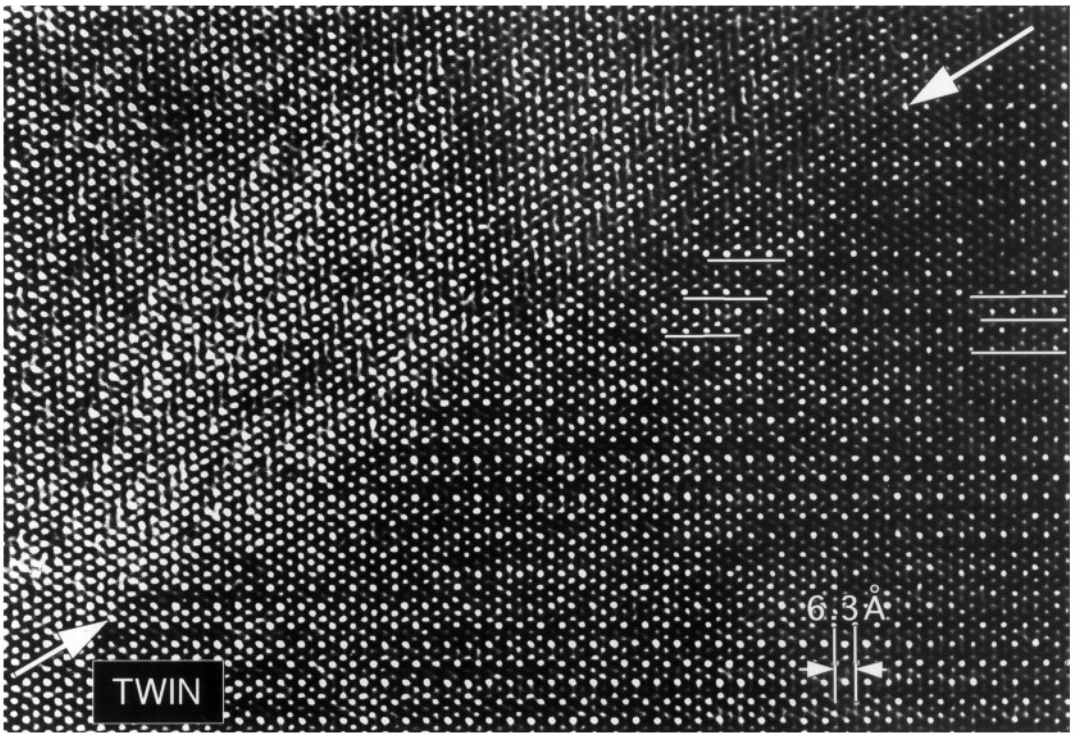

FIG. 14. Crystal area of $TaSi_xTe_2$ containing two orientation variants. One of the orientation variants contains two translation variants. The positions of the dark lines in the two domains are indicated.

spot intensity away from the basic spots supports the view that this $8c_0$ period is not well defined and results from the average of $7c_0$ and $9c_0$. The corresponding HREM (Fig. 20) suggests a possible model. Assuming the dark lines in Fig. 20 to reveal the OPBs, the model of Fig. 21 can be deduced, where the mixture of $7c_0$ and $9c_0$ spacings is

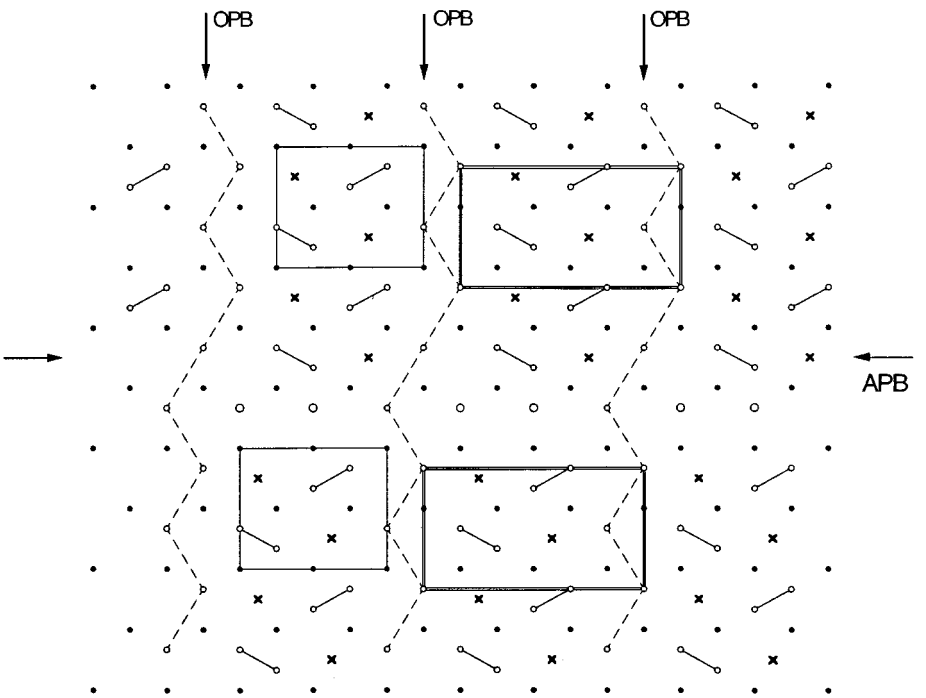

FIG. 15. Model for the boundary between translation variants of the LPSS.

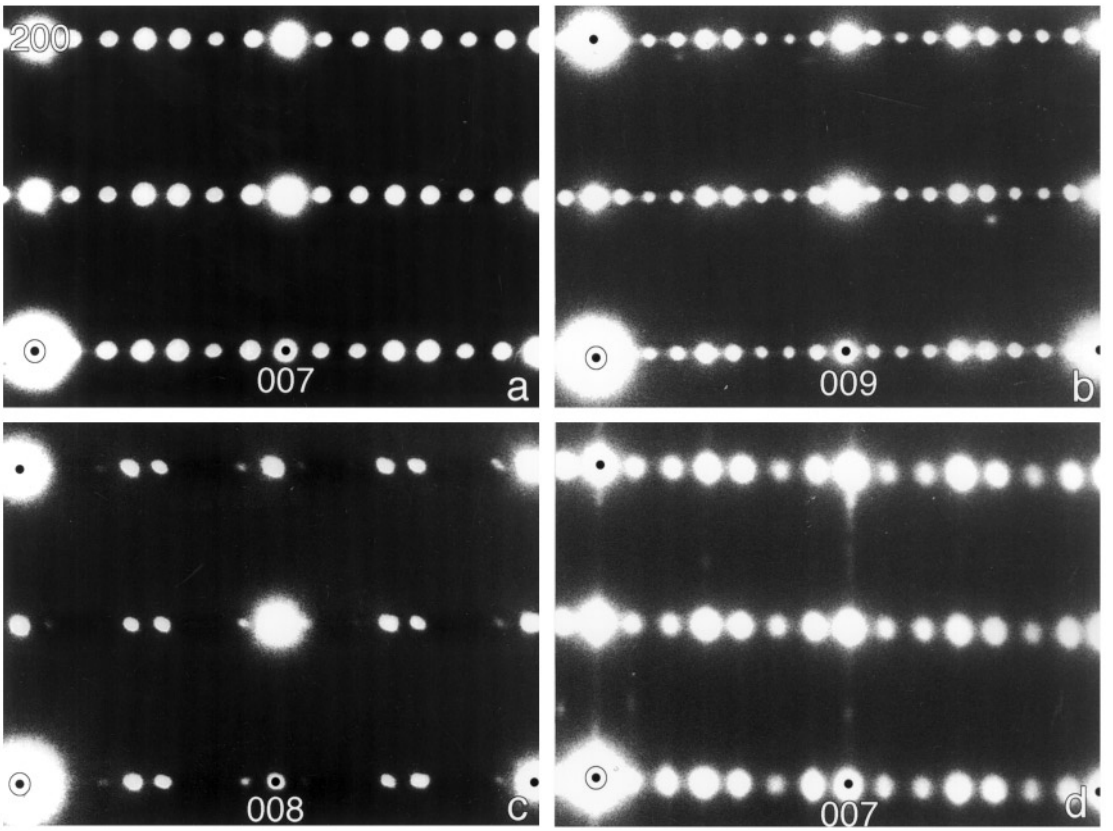

FIG. 16. [010] diffraction patterns of different commensurate LPSS in Si_xNbTe_2 ($x = 3/7$). (a) The spot distance 000–$(002)_{Te}$ is divided in 14 intervals by LPSS spots ($x = 3/7$). (b) The spot distance 000–$(002)_{Te}$ is divided in 18 intervals ($x = 4/9$). (c) The spot distance 000–$(002)_{Te}$ is divided in 16 intervals ($x = 0.436$). (d) Pattern exhibiting streaking along [100]*.

uniform. The stacking also accounts for the apparent width and spacing of the OPB regions as observed in high-resolution images.

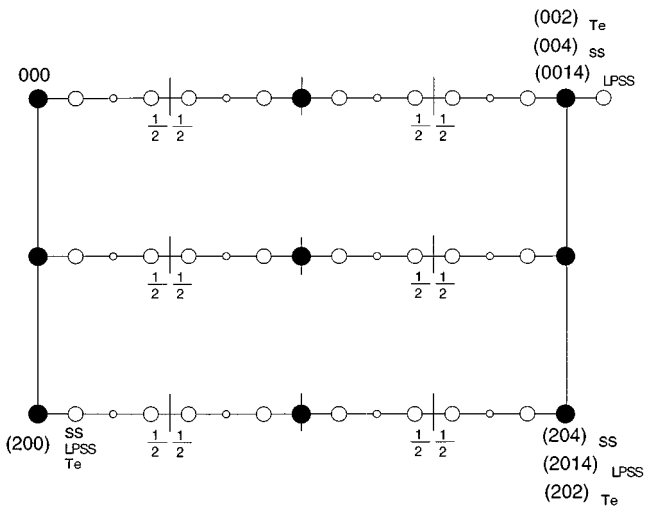

FIG. 17. Schematic diffraction pattern corresponding to Fig. 16a. The intensity distribution is represented by the size of the dots. The indices refer to different reference frames.

The variability in spacing observed in $Si_{3/7}NbTe_2$ is presumably the result of some inhomogeneity in the silicon distribution and hence of the zig-zag lines of isolated Nb.

Image Simulations

In order to specify the stacking of successive sandwiches in the LPSS, computer simulations were performed for various plausible stacking modes, in accordance with the AABB stacking principle of the tellurium sublattice. The displacement vectors relating the two sandwiches can be formulated as $\bar{R} = -1/3\bar{a}_0 + 1/2\bar{b}_0 + \bar{r}_j$ where $\bar{r}_j$ are symmetry translations of the tellurium sublattice, but not of the cation sublattices. This gives rise to six possible stacking modes. Six more stacking variants are obtained if one of the sandwiches is allowed to be rotated over 180° about an axis parallel to the b axis with respect to the other one. The orthorhombic symmetry makes 60° and 120° rotations incompatible with the structure.

We note that the observed hexagonal dot pattern (Fig. 6) along the [010] zone exhibits bright dots situated on a centered rectangular lattice with mesh size $a_0 \times 3a_0$, as well as dots of smaller brightness. The whole pattern lacks

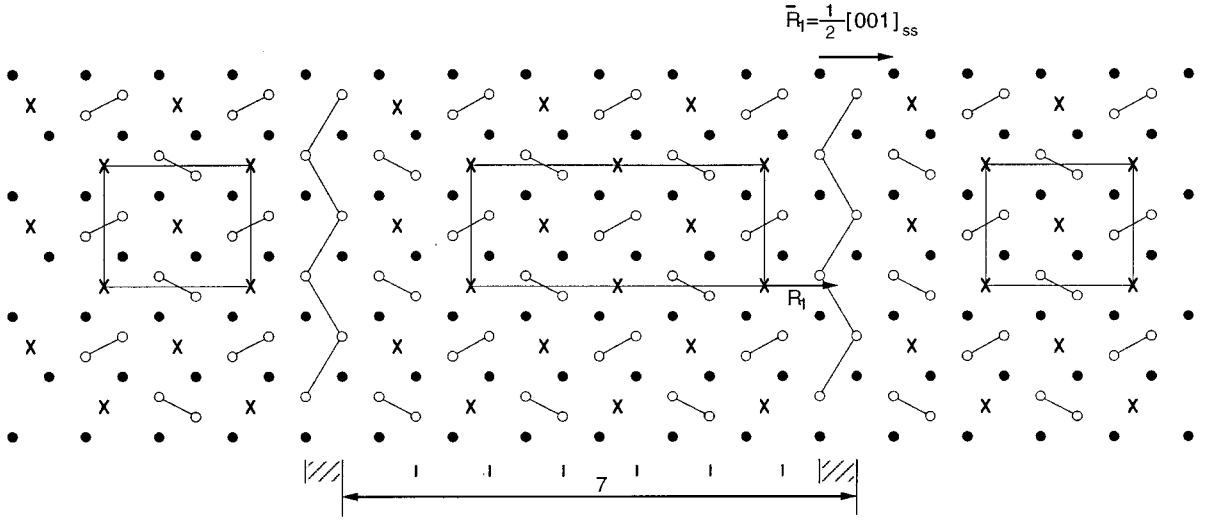

FIG. 18. Model for the LPSS, producing a diffraction pattern as in Fig. 16a. The successive OPB are separated by the width of seven Te sublattice unit cells ($7c_0$). All OPBs are equivalent and "in phase." In $Si_{4/9}NbTe_2$, these strips would have a width of $9c_0$.

a center of symmetry. This observation allows us to eliminate stackings which are centrosymmetrical in projection because these would produce a centrosymmetrical configuration of bright dots.

The model which leads to the best correspondence between observed and simulated dot pattern is one in which the two sandwiches are related by a pure displacement $\bar{R} = 1/6\bar{a}_0 + 1/2\bar{b}_0 + 3/2\bar{c}_0$. The projection along [010] of this structure is not centrosymmetric. The corresponding simulated image for a thickness of 49 Å and a single defocus value (−1000 Å) is shown in Fig. 22.

DISCUSSION

In discussing the crystal structure of Si_xTaTe_2 and its relation to the diffraction pattern, we used different reference frames. It should be noted that when applying the fractional shift method (8), it is essential to use corresponding reference frames for direct ($\bar{R}$) and reciprocal ($\bar{g}$) lattice when computing the fractional shift $\bar{g}\cdot\bar{R}$. In Fig. 23 the diffraction patterns have been indexed with reference to the various unit meshes with a different c parameter; when using different reference frames, the third index obviously changes.

In our discussion, we used the following terminology:

(i) the tellurium sublattice with mesh size $a_0 \times c_0$ ($a_0 = 6.329$ Å; $c_0 = 3.8258$ Å) (Fig. 23a)

(ii) the superstructure lattice (SS) with mesh size $a_0 \times 2c_0$ (Fig. 23b)

(iii) the long-period superlattice (LPSS): $a_0 \times 3c_0$ (Fig. 23c)

(iv) the very-long-period superlattice (VLPSS): $a_0 \times 14.5c_0$ (Fig. 5b)

This last structure is the actually observed structure of Si_xTaTe_2, the others are used as intermediate steps to build up a model for the VLPSS.

The tellurium substructures and superstructure (SS) are shown in Fig. 1. The out-of-phase boundary has a displacement vector $\bar{R}_1 = (1/2)[001]_{SS}$ when referred to the SS. The LPSS consists of strips three tellurium sublattice unit-cells wide ($3c_0$). Within the strips, the structure is the SS with unit mesh $a_0 \times 2c_0$. These strips are all separated by OPB with displacement vector $\bar{R}_1$. This is an idealized LPSS which would produce diffraction spots at the sites marked by short bars in Fig. 5b; it would be a commensurate structure. However, in actual fact, the structure produces an incommensurate diffraction pattern also represented schematically in Fig. 5b; it suggests the presence of a very-long-period superstructure (VLPSS) with a period which is the inverse of the satellite spacing [i.e., $(1/14.5)c_0^*$].

Such a VLPSS can be considered as a superstructure of the LPSS formed by the periodic introduction of interfaces with a displacement vector $\bar{R}_2 = (1/6)[301]$ with respect to the LPSS and consisting of four strips with a width $3c_0$ and one strip with a width $2.5c_0$, as shown in Figs. 3 and 24 (or alternatively formulated with a width of four times six interrow distances of the Te sublattice followed by one strip of five interrow distances). The proposed displacement vector $\bar{R}_2 = (1/6)[301]_{LPSS}$ is a lattice vector of the tellurium sublattice but not of the LPSS; it causes the correct fractional shifts, the correct interspot spacing, and the correct displacement of the dot rows along $[101]_{LPSS}$ in the high-resolution image because [101]. (1/6)[301] = 1/3 (mod. 1).

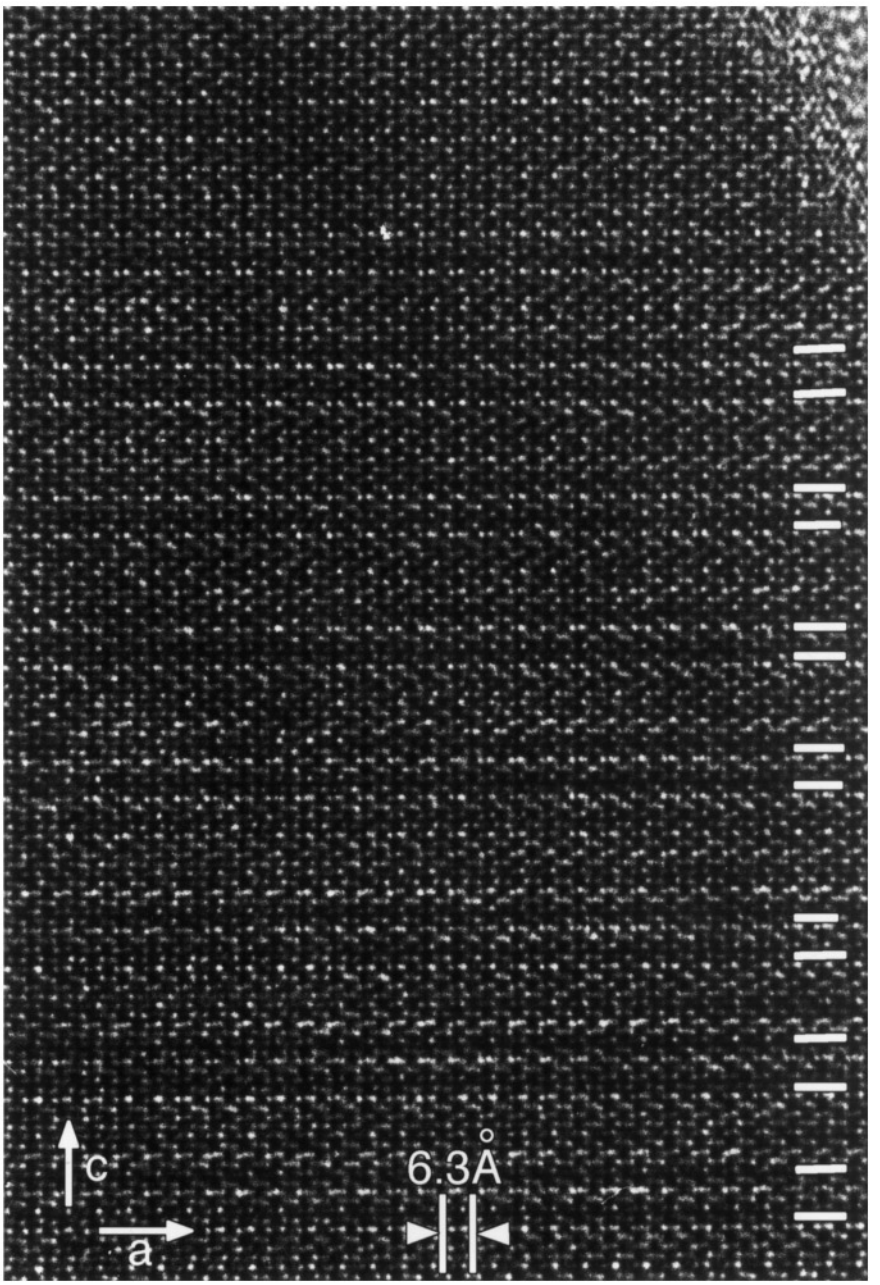

FIG. 19. High-resolution image of $Si_{3/7}NbTe_2$ along the [010] zone exhibiting pairs of "dark lines" suggesting the arrangement of "zig-zag" lines in successive sandwiches as also represented in Fig. 24c.

An alternative reasoning would consist in considering the VLPSS as a structure with an average period of $1/5(4 \times 3c_0 + 1 \times 2.5c_0) = 2.9c_0$. The satellites would then be sequences associated with the basic spots of the SS and exhibit a spacing anomaly.

Both interpretations lead to the same model, but the former reasoning is the more stringent test because it requires the fitting of two parameters: the period and the fractional shifts.

In Si_xNbTe_2, the observed numbers of tellurium unit cells in the strips are even (6, 8). If it would be odd, there would be no phase shift between the structures in the strips because $\bar{R}$ would be a lattice vector of the LPSS. The period 8 can thus only be realized as a mixture of 7 and 9. This mixture was not quite uniform in Fig. 16c, which results in a rapid decrease in intensity of the satellites on both sides of the basic spot positions. Furthermore, because in these structures the strips of superstructure are all an integer

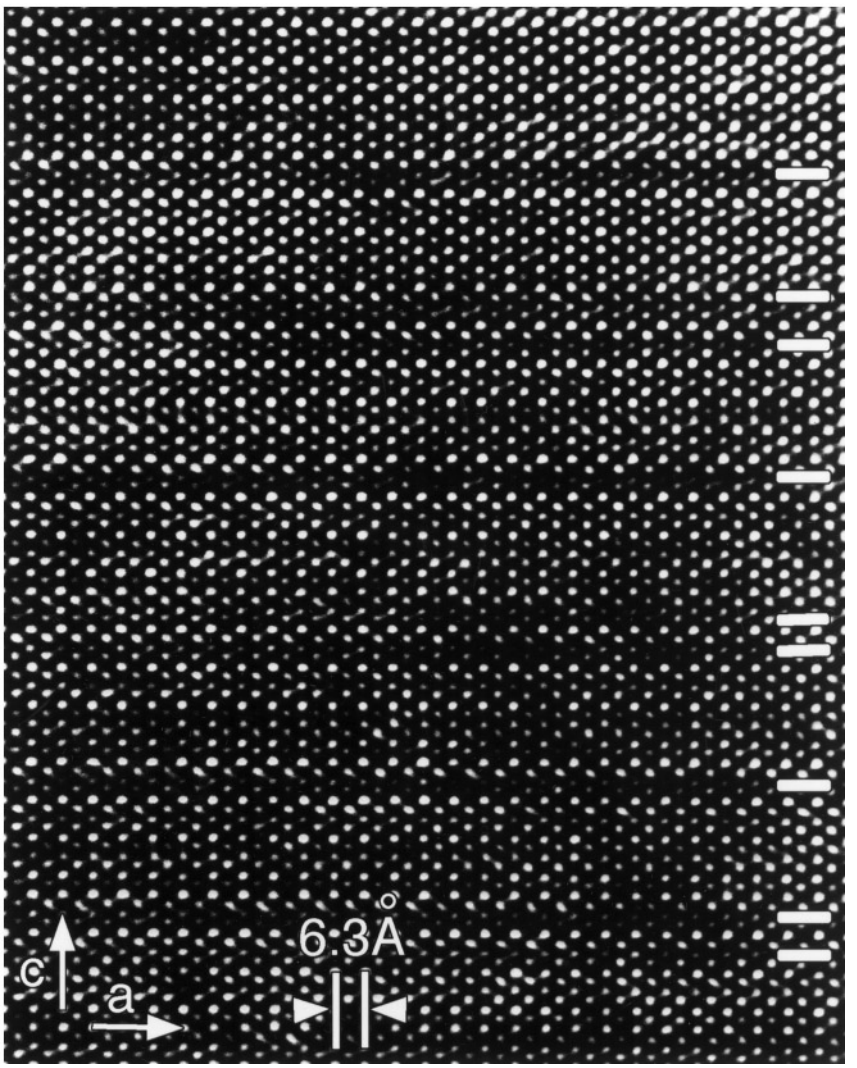

FIG. 20. High-resolution image exhibiting a uniform mixture of two periods $7c_0$ and $9c_0$ in $Si_{3/7}NbTe_2$. A model of the layer arrangement responsible for this image is shown in Fig. 21. The OPBs are imaged as darker lines.

number of unit cells wide, no lateral displacement of the fringes occurs at any of the OPBs, as experimentally observed under high-resolution conditions in Figs. 20 and 21.

The stacking of successive lamellae cannot be deduced in an unambiguous straightforward manner from the images; nevertheless, some reasonable suggestions can be deduced from these images.

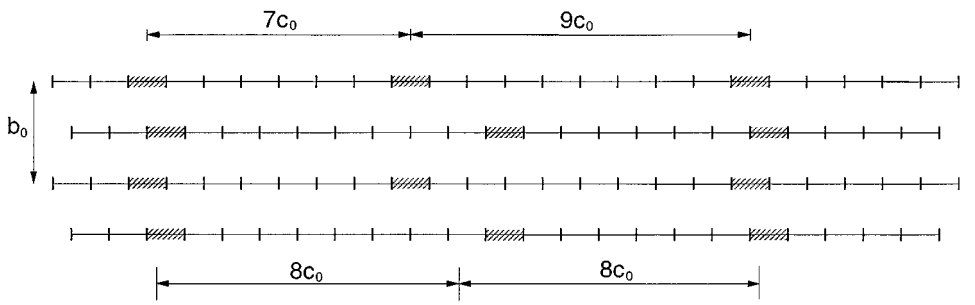

FIG. 21. Cross-sectional view of a model for the arrangement of layers in $NbSi_{3/7}Te_2$ producing a long period of $8c_0$. The cross-hatched line segments represent the OPBs. The arrangement is a uniform mixture of two periods $9c_0$ and $7c_0$. This model is inspired by Fig. 20.

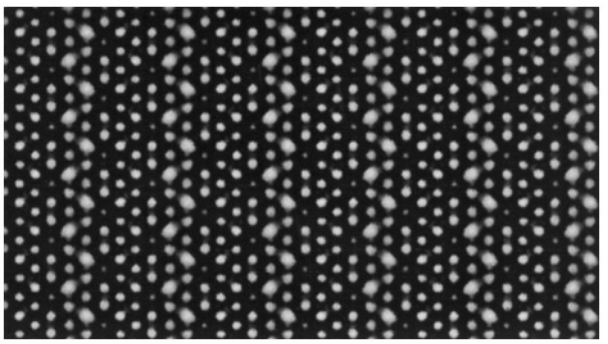

FIG. 22. Computer simulated HREM image along the [010] direction for a thickness of 49 Å and a focus value of −600 Å, based on the model of Fig. 6a.

Intuitively one would expect the OPB lines to alternate in successive sandwiches as shown in Fig. 25a. This is the most symmetrical arrangement; it would lead to centering of the *h*0*l* zone pattern. The structures in the two sandwiches would then be related by a displacement vector $[\bar{R} = -1/3\bar{a} + 1/2\bar{b} + 1/2\bar{c}]_{\mathrm{LPSS}}$. It would cause extinctions for l = odd along the 00*l* spot row in the [010] zone diffraction pattern of the LPSS, which is not observed in the Nb compounds.

The simplest alternative would be to assume successive sandwiches to be stacked as vertically as is compatible with the stacking of the Te sublattice. In this way walls of OPB lines would result (Fig. 25b).

High-resolution images along the [010] zone of Si_xNbTe_2 exhibit equally spaced singular lines of dots parallel to *a* (Figs. 19 and 20), with a line spacing equal to the long-period spacing along *c* deduced from the diffraction pattern. It is therefore logical to assume that these lines image OPB lines, just as is the case for Si_xTaTe_2 in Fig. 7.

In certain Nb compounds the *c*-period contains a single such line; in other cases the *c*-period contains two such lines (Fig. 19). In the latter case, it is therefore tempting to associate the two lines of a pair with the positions of the OPB lines in the two sandwiches in the unit cell. The stacking corresponding to Fig. 19 might thus be as shown schematically in Fig. 24c.

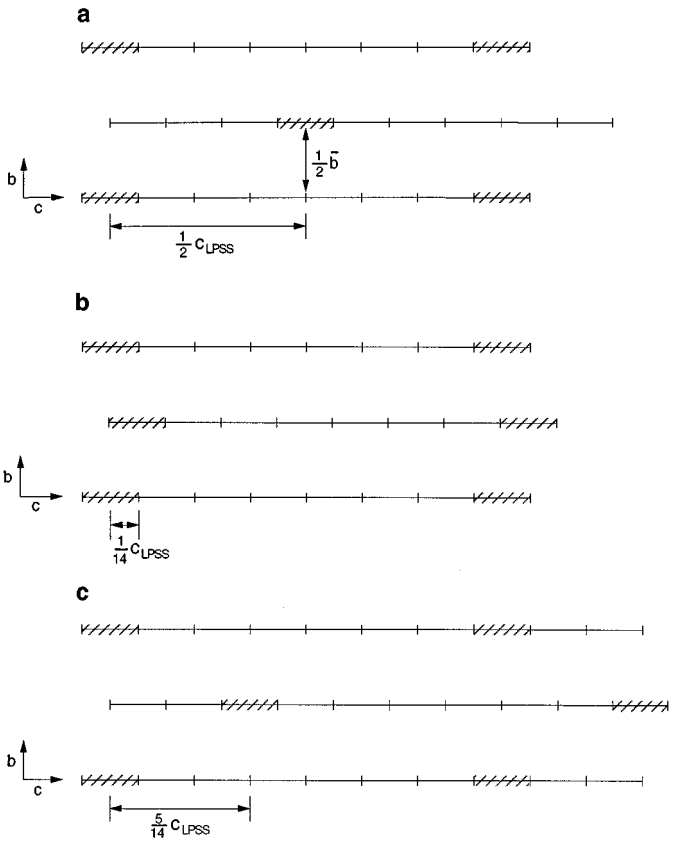

FIG. 24. Schematic representation of the very long period superstructure (VLPSS) of Si_xTaTe_2 which is compatible with the diffraction pattern of Fig. 5a.

The structural model for the long-period superstructures in Si_xTaTe_2 is consistent with all diffraction effects: it leads to the correct spot geometry and relative intensities in the apparently incommensurate diffraction pattern and it leads to the observed image characteristics in high-resolution images: in particular, to the observed 2/3 lateral shift of the $[101]_{\mathrm{LPSS}}$ atom rows with the correct periodicity of the shift lines. It leads also to an Si enrichment of the compound (i.e., to $x > 1/3$), which is consistent with the overall prepared composition and with the observed *q*-vector.

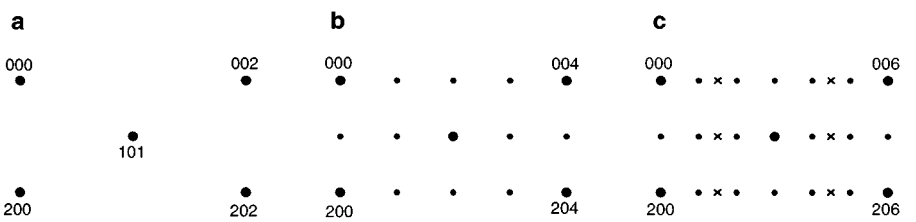

FIG. 23. Schematic representation of various diffraction patterns. (a) basic Te sublattice. (b) basic superstructure of $A_{0.5}MTe_2$. (c) long-period superstructure of $A_{0.33}MTe_2$.

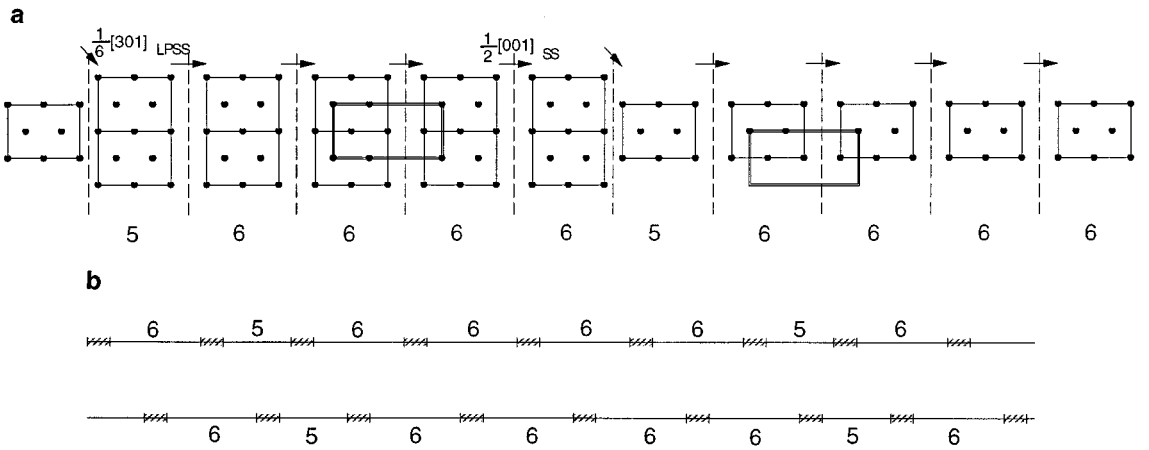

FIG. 25. Possible arrangements of the stacking of sandwiches such as present in $Si_{3/7}NbTe_2$. (a) Most symmetrical arrangement. (b) Best approximation to a vertical arrangement. (c) Arrangement suggested by the high resolution image of Fig. 19.

ACKNOWLEDGMENTS

N. Frangis is grateful to the European Commission for a training grant (ERBCHBICT 941798).

REFERENCES

1. A. van der Lee, M. Evain, M. Mansuetto, L. Monconduit, R. Brec, and J. Rouxel, *J. Solid State Chem.* **111,** 75 (1994).
2. Jing Li, Michael E. Badding, and F. J. DiSalvo, *J. Alloys and Compounds* **184,** 257 (1992).
3. L. Monconduit, M. Evain, F. Boucher, R. Brec, and J. Rouxel, *Z. Anorg. Allg. Chem.* **616,** 177 (1992).
4. M. Evain, L. Monconduit, A. van der Lee, R. Brec, J. Rouxel, and E. Canadell, *Nouv. J. Chem.* **8,** 215 (1994).
5. L. Monconduit, M. Evain, R. Brec, J. Rouxel, and E. Canadell, *C.R. Acad. Sci. Paris* **316,** II, 25 (1993).
6. A. van der Lee, M. Evain, L. Monconduit, R. Brec, and S. van Smaalen, *J. Phys. Condens. Matter* **6,** 933 (1994).
7. A. van der Lee, M. Evain, L. Monconduit, R. Brec, J. Rouxel, and V. Petricek, *Acta Cryst. B* **50,** 119 (1994).
8. J. Van Landuyt, R. De Ridder, R. Gevers, and S. Amelinckx, *Mat. Res. Bull.* **5,** 353 (1970).
9. J. Van Landuyt, G. Remout, and S. Amelinckx, *Phys. Stat. Sol.* (*a*) **41,** 271 (1970).
10. C. Manolikas and S. Amelinckx, *Phys. Stat. Sol.* (*a*) **60,** 607 (1980); **61,** 179 (1980).
11. C. Manolikas, J. Van Landuyt, and S. Amelinckx, *Phys. Stat. Sol.* (*a*) **53,** 327 (1979).
12. G. Van Tendeloo and S. Amelinckx, *Acta Cryst. A* **30,** 431 (1974).
13. J. Sapriel, *Phys. Rev. B* **12,** 5128 (1975).